

## Research Article

# A monitoring campaign (2013–2020) of ESA’s Mars Express to study interplanetary plasma scintillation

P. Kummamuru<sup>1</sup>, G. Molera Calvés<sup>1</sup>, G. Cimò<sup>2</sup>, S. V. Pogrebenko<sup>2</sup>, T. M. Bocanegra-Bahamón<sup>3</sup>, D. A. Duev<sup>4</sup>, M. D. Md Said<sup>2</sup>, J. Edwards<sup>1</sup>, M. Ma<sup>5</sup>, J. Quick<sup>6</sup>, A. Neidhardt<sup>7</sup>, P. de Vicente<sup>8</sup>, R. Haas<sup>9</sup>, J. Kallunki<sup>10</sup>, G. Maccaferri<sup>11</sup>, G. Colucci<sup>12</sup>, W. J. Yang<sup>13</sup>, L. F. Hao<sup>14</sup>, S. Weston<sup>15</sup>, M. A. Kharinov<sup>16</sup>, A. G. Mikhailov<sup>16</sup> and T. Jung<sup>17</sup>

<sup>1</sup>School of Natural Sciences, University of Tasmania, Private Bag 37, Hobart, TAS 7005, Australia, <sup>2</sup>Joint Institute for VLBI-European Research Infrastructure Consortium, Oude Hogeveendijk 4, 7991, PD Dwingeloo, The Netherlands, <sup>3</sup>Jet Propulsion Laboratory, Pasadena, CA 91109, USA, <sup>4</sup>California Institute of Technology, Pasadena, CA 91125, USA, <sup>5</sup>Shanghai Astronomical Observatory, 80 Nandan Road, Shanghai, People’s Republic of China, <sup>6</sup>Hartebeesthoek Radio Astronomy Observatory, Krugersdorp, South Africa, <sup>7</sup>Technical University of Munich, Research Facility Satellite Geodesy, Geodetic Observatory Wettzell, Sackenrieder Str. 25, D-93444 Bad Kötzing, Germany, <sup>8</sup>Observatorio de Yebes (IGN), Yebes, Guadalajara, Spain, <sup>9</sup>Chalmers University of Technology, Onsala Space Observatory, Göteborg, Sweden, <sup>10</sup>Aalto University Metsähovi Radio Observatory, Kylmäla, Finland, <sup>11</sup>National Institute for Astrophysics, Radio Astronomy Institute, Radio Observatory Medicina, Medicina, Italy, <sup>12</sup>E-geos S.p.A, Space Geodesy Center, Italian Space Agency, Matera, Italy, <sup>13</sup>Xinjiang Astronomical Observatory, Chinese Academy of Sciences, Urumqi, People’s Republic of China, <sup>14</sup>Yunnan Astronomical Observatory, Chinese Academy of Sciences, Kunming, People’s Republic of China, <sup>15</sup>Institute for Radio Astronomy & Space Research (IRASR) School of Engineering, Computer and Mathematical Sciences, Faculty of Design and Creative Technologies, Auckland University of Technology, Auckland, New Zealand, <sup>16</sup>Institute of Applied Astronomy of Russian Academy of Sciences, St Petersburg, Russia and <sup>17</sup>Korea Astronomy & Space Science Institute, 776 Daedeok-daero, Yuseong-gu, Daejeon, South Korea

### Abstract

The radio signal transmitted by the Mars Express (MEX) spacecraft was observed regularly between the years 2013–2020 at X-band (8.42 GHz) using the European Very Long Baseline Interferometry (EVN) network and University of Tasmania’s telescopes. We present a method to describe the solar wind parameters by quantifying the effects of plasma on our radio signal. In doing so, we identify all the uncompensated effects on the radio signal and see which coronal processes drive them. From a technical standpoint, quantifying the effect of the plasma on the radio signal helps phase referencing for precision spacecraft tracking. The phase fluctuation of the signal was determined for Mars’ orbit for solar elongation angles from 0 to 180 deg. The calculated phase residuals allow determination of the phase power spectrum. The total electron content of the solar plasma along the line of sight is calculated by removing effects from mechanical and ionospheric noises. The spectral index was determined as  $-2.43 \pm 0.11$  which is in agreement with Kolmogorov’s turbulence. The theoretical models are consistent with observations at lower solar elongations however at higher solar elongation ( $>160$  deg) we see the observed values to be higher. This can be caused when the uplink and downlink signals are positively correlated as a result of passing through identical plasma sheets.

**Keywords:** spacecraft tracking – space weather – plasma – solar wind – interferometry

(Received 10 December 2022; revised 13 February 2023; accepted 19 February 2023)

### 1. Introduction

The last several decades have seen a significant number of spacecraft launched to explore the Solar System. Techniques like very long baseline interferometry (VLBI) and Doppler spacecraft tracking have progressively been used over the same period for different space science missions. The Planetary Radio Interferometry and Doppler Experiment (PRIDE) programme was developed by the Joint Institute for Very Long Baseline Interferometry European Research Infrastructure Consortium (JIVE) which uses the VLBI and Doppler techniques to conduct radio science experiments for scientific and orbit determination purposes. Guifré Molera Calvés

et al. (2021) describes the software which was key to single dish data processing of spacecraft signals with VLBI telescopes. The software was key in the observations of Venus Express’ (VEX) (Duev et al. 2012) and MEX Phobos flyby (Duev et al. 2016) for ultra-precise orbit determination. PRIDE has been used in several other science experiments; the study of interplanetary phase scintillation using spacecraft signals from VEX (Molera Calvés et al. 2014), noise budget estimation of the MEX Phobos flyby (Bocanegra-Bahamón et al. 2017), radio occultation experiment with the ESA’s Venus express (VEX) to study Venus’ atmosphere (Bocanegra-Bahamón et al. 2019). The technique will play a crucial role in the upcoming European Space Agency’s (ESA) Jupiter Icy Moons Explorer (JUICE) mission scheduled to launch in 2023.

The characterisation of interplanetary plasma is a crucial component for achieving high-precision astrometry with the PRIDE technique. The presence of interplanetary plasma is a result of the outflow of ionised particles from the Sun known as solar winds. Solar winds are broadly classified based on their speeds into slow and fast solar winds. Slow solar winds are characterised by speeds

**Corresponding author:** P. Kummamuru, email: [pradyumna.kummamuru@utas.edu.au](mailto:pradyumna.kummamuru@utas.edu.au).

**Cite this article:** Kummamuru P, Molera Calvés G, Cimó G, Pogrebenko SV, Bocanegra-Bahamón TM, Duev DA, Md Said MD, Edwards J, Ma M, Quick J, Neidhardt A, de Vicente P, Haas R, Kallunki J, Maccaferri G, Colucci G, Yang WJ, Hao LF, Weston S, Kharinov MA, Mikhailov AG and Jung T. (2023) A monitoring campaign (2013–2020) of ESA’s Mars Express to study interplanetary plasma scintillation. *Publications of the Astronomical Society of Australia* 40, e013, 1–12. <https://doi.org/10.1017/pasa.2023.12>

© The Author(s), 2023. Published by Cambridge University Press on behalf of the Astronomical Society of Australia. This is an Open Access article, distributed under the terms of the Creative Commons Attribution licence (<http://creativecommons.org/licenses/by/4.0/>), which permits unrestricted re-use, distribution and reproduction, provided the original article is properly cited.

between 300 and  $-500 \text{ km s}^{-1}$  and higher density of  $\sim 10^7 \text{ cm}^{-3}$ . Their origins are not fully understood but some of the major models explaining the origin of the slow solar winds are the coronal flux tube expansion phenomenon (e.g. Pinto & Rouillard 2017) and the interchange magnetic reconnection (e.g. Edmondson 2012). Fast solar winds have speeds ranging from 600 to  $800 \text{ km s}^{-1}$  with lower densities compared to slow solar winds with a value around  $5 \times 10^5 \text{ cm}^{-3}$ . The fast solar winds originate from the coronal holes, regions of open magnetic field lines that propel matter into space (Hassler *et al.* 1999).

A spacecraft communications telemetry signal is affected by multiple factors along the propagation path including the motion of the spacecraft, the characteristics of the antenna, the helioplasm, Earth's ionosphere, and spacecraft and antenna system noises. These affect the observables of the spacecraft signal including signal frequency, phase and amplitude. The amplitude of a signal is significantly disrupted when the line of sight is close to the Sun (Manoharan *et al.* 1995) such as a solar conjunction. The automatic gain control (AGC) is always switched on in our experiments. The AGC provides a controlled received amplitude facilitating easier signal processing with less changes in the dynamic range. Due to the two aforementioned reasons, the amplitude of the signal is not a suitable metric in comparison to the more precisely detected phase. The solar wind introduces frequency (Wexler *et al.* 2019) and phase fluctuations in the signal. These fluctuations become larger when observations are closer to the Sun or during coronal mass ejections events. We observe spacecraft downlink signals operating in a coherent communication mode where the spacecraft generates a downlink signal coherent with the transmitted ground station uplink, offering increased phase stability. We then analyse the phase fluctuations of the spacecraft carrier signal to characterise the impact of interplanetary plasma.

Molera Calvés *et al.* (2014) determined the phase fluctuation indices of VEX's telemetry signal along Venus' orbit between the years of 2009–2013 for solar elongation angles over the range of 0–45 deg. In this study, we use the telemetry signal of MEX to observe the phase fluctuations over a larger extent of solar elongation angles 0–180 deg to get a more extensive coverage. Using the phase fluctuation spectrum we determined from our Doppler observations, we calculate the total electron content (TEC) along the sightlines to Mars. The extended observing campaign of nearly 3 orbital periods of Mars allows us to confirm the solar density profile across the entire span of solar elongation. Observations at higher solar elongations are essential to extend and improve current theoretical models of the TEC of interplanetary plasma.

The relevance of studying the phase spectrum of plasma extends to the PRIDE's experiment of tracking spacecraft using the VLBI-phase referencing technique. In this technique, telescopes, while tracking, switch sources between the spacecraft and flux calibrators which are ideally separated by only a few degrees. When alternating from one target to the other, one of the key parameters is the nodding cycle, the time spent on observing the spacecraft and the calibrator and the switching time between targets. The nodding interval between sources has to be adjusted so that the path length change due to the phase errors is  $< \lambda/4$  where  $\lambda$  is the wavelength of the signal (Beasley & Conway 1995). The measured phase fluctuations are a symptom of noise errors introduced in the radio signal due to the propagation media; quantifying this would allow us to select optimum nodding cycles. This consequentially enables the precise determination of the spacecraft's state vectors.

In the next part of the paper, we discuss the theory of phase scintillation spawning through the interplanetary plasma region.

This is followed up by an overview of the observations taken over the full campaign and the methodologies used for the data processing. In section four, we demonstrate our results and compare them with previous results. In section five, we discuss the implications of our results and recognise the avenues for improvement for future studies.

## 2. Theory

The upper atmosphere of the Sun, the corona, is responsible for releasing a stream of plasma which is the solar wind. The solar wind plasma overlaid with the heliospheric magnetic field (Owens & Forsyth 2013) permeates through the interplanetary medium. When radio signals are sent to and from spacecraft they pass through the interplanetary plasma and as a consequence we observe fluctuations in the signal. The scattering regime of the plasma is modelled in different ways based on geometry and distance and can be understood to have weak and strong scattering zones. A majority of the solar wind scattering is in the weak regime while it enters into the strong regime closer to the Sun (Narayan 1992). In the weak scattering domain, the fluctuations are caused due to the electron density variations in the solar wind which scatter the radio waves. The distortions in the phase fronts are dependent on the size of the plasma irregularities which can be both diffractive and refractive with the latter associated with smaller irregularities (Boyde *et al.* 2022). Conroy *et al.* (2022) delves further on distinguishing refractive and diffractive phase scintillation.

Consolidating a quantitative relationship between the scintillation and the plasma density will help us get a better insight into the solar wind structure and thereby, the corona. The fluctuations we observe in our radio signal is a consequence of large-scale structure of the solar wind (Schwenn 1990). We look at how the expanse of the inhomogeneous medium translates to the electron density across the line of sight of our observations.

The phase scintillation provides information on the full range of scale sizes for electron density variations at different distances and is typified by the refractive index. The inhomogeneous medium of plasma spans across thousands of kilometres (Yakovlev 2002) and is characterised by a spectrum of refractive coefficients given by

$$\phi_n(\kappa) = 0.033c_n^2(\kappa^2 + \kappa_0^2)^{-\alpha/2} \exp\left(-\frac{\kappa^2}{\kappa_m^2}\right) \quad (1)$$

where  $k = 2\pi/\lambda$  represents the spatial wave number,  $\kappa$  is the scale of the plasma irregularity that the signal traverses,  $\kappa_m$  and  $\kappa_0$  are spatial wave numbers in the outer and inner scales of the refractive index regularities,  $\alpha$  is the plasma irregularity's spatial spectrum index, and  $c_n$  is the plasma irregularity's structural coefficient. The radio wave fluctuations are proportional to the spatial spectrum of the refractive index with the fluctuations in the phase being more pronounced than the amplitude. The variance of the phase of the fluctuations is calculated as

$$\sigma_\psi^2 = (2\pi\nu)^2 \int_0^L \int_0^{\kappa_0} \phi_n(\kappa) \kappa d\kappa dx \quad (2)$$

where  $\nu$  is the wavenumber of the wave travelling through vacuum. We integrate over the satellite to Earth path length ( $L$ ) and the extent of the wavenumber of the plasma inhomogeneity spectrum ( $\kappa$ ) from 0 to  $2\pi\Lambda_0^{-1}$  ( $\Lambda = 10^6 \text{ Km}$  is the outer turbulence scale) (Yakovlev 2002).

In this work, we determine the phase scintillation as the standard deviation of the phase residual values. The phase residuals are

extracted from fine Doppler detection of the carrier signal and is the quantity obtained after compensating residual phase rotation. The phase residuals are used to construct the phase power spectrum which gives us a qualitative and quantitative insight into the interplanetary plasma.

Another measure of the effects of the propagation on the radio signal is the TEC, expressed in electrons per square metre; one TEC unit (tecu) is  $10^{16}$  electrons  $m^{-2}$ . The TEC is calculated as a line integral along the line of sight from the Earth to a spacecraft as follows

$$TEC = \frac{1}{tecu} \sum_{s=E}^{SC} N_e(s) \cdot d_{seg} \quad (3)$$

where E represents the position of the Earth in a 2D map and SC the position of the spacecraft,  $N_e$  is the electron column density function of the solar wind with respect to the Sun normalised by  $tecu$ , and  $d_{seg}$  is the distance increment determined by the number of intervals of the line of sight between observer-target. The electron density is integrated along the path length and is given for the nominal, slow, and fast solar winds as follows (Ando et al. 2015):

$$N_{nominal} = 5 \times 10^6 \cdot (AU/d)^2 m^{-3}, \quad (4)$$

$$N_{slow} = (4.1 \cdot s_{dist}^{-2} + 23.53 \cdot s_{dist}^{-2.7}) \cdot 10^{11} + (1.5 \cdot s_{dist}^{-6} + 2.99 \cdot s_{dist}^{-16}) \cdot 10^{14}, \quad (5)$$

$$N_{fast} = (1.155 \cdot s_{dist}^{-2} + 32.2 \cdot s_{dist}^{-4.39} + 3254 \cdot s_{dist}^{-16.25}) \cdot 10^{11}, \quad (6)$$

where  $d$  is the solar offset (in metres) and  $s_{dist}$  is the ratio of solar offset and the radius of the Sun.

The signal is also affected by ionospheric and tropospheric contributions along its path (Crane 1977; Karasawa, Yamada, & Allnutt 1988). The ionospheric induced phase delay is given by

$$I = -\frac{f_p \times TEC}{f^2} \quad (7)$$

where  $f_p = 8.98\sqrt{N}$  (Hz) is the frequency of the plasma medium (Davies 1990) and  $f$  is the transmission frequency. The phase delay of the signal in cycles is determined by dividing the ionospheric path contribution by the wavelength,  $L = I/\lambda$ .

Radio links are subject to tropospheric scintillation due to refractive index fluctuations. The refraction has both wet and dry components with the latter largely dominant (90%) and well correlated with the atmospheric pressure making it easy to determine (Jin et al. 2007). The delay due to the wet component is highly variable because of the rapidly fluctuating water vapour content in the atmosphere. The accurate modelling of the wet component contribution relies on the use of high quality radiosondes like the Topex (Keihm, Janssen & Ruf 1995) which is infeasible for every area of science unless it is high-precision GPS work, thus we rely on mathematical models. However, the signal attenuation increases at higher microwave frequencies ( $> 10$  GHz) and as a consequence we lose any benefits of atmospheric refraction at this stage (Vasseur 1999; Smyth & Trolese 1947). The atmospheric delay is higher at lower elevations because of how it is proportional to  $1/\sin \epsilon$  where  $\epsilon$  is the elevation angle (MacMillan & Ma 1994). However, the root mean square (*rms*) of tropospheric induced phase fluctuation is negligible compared to the solar wind

**Table 1.** Overview of the telescopes used for our observations of ESA MEX spacecraft, their locations, SEFD values, and the diameter of the main parabolic dish.

Antenna (code)	Country	SEFD(Jy)	$\phi$ (m)
Ceduna (Cd)	Australia	600	30
Hobart (Ho)	Australia	2 500	26
Katherine (Ke)	Australia	3 500	12
Yarragadee (Yg)	Australia	3 500	12
Hobart (Hb)	Australia	3 500	12
Svetloe (Sv)	Russia	350	32
Zelenchuk (Zc)	Russia	350	32
Badary (Bd)	Russia	350	32
Tianma (T6)	China	200	65
Yeibes (Ys)	Spain	200	40
Hartebeesthoek (Ht)	South Africa	3 000	15
Warkworth (Ww)	New Zealand	3 500	12
Kunming (Km)	China	1 500	40
Sheshan (Sh)	China	1 500	12
Metsahovi (Mh)	Finland	3 200	14
Hartebeesthoek (Hh)	South Africa	3 000	26
Onsala (On)	Sweden	1 500	20
Wetzell (Wz)	Germany	750	20
Wetzell (Wn)	Germany	1 400	13.2
Warkworth (Wa)	New Zealand	900	30
KVN Ulsan (Ku)	South Korea	1 080	21

value (Acosta, Nessel, & Morse 2010; Holdaway et al. 1995) while we tend to ignore the lower elevation observations ( $< 10$  deg) due to tropospheric saturation.

### 3. Observational summary

#### 3.1 Observations

The observing campaign was held across 303 epochs with a total of 504 sessions using 22 different radio telescopes around the world. Table 1 shows a description of antennas, station code, geographical location, the system equivalent flux density (SEFD), and the dish size used in the observations. These antennas all are equipped with a receiver capable to operate at X-band frequencies. Although, the system noise of the antenna (expressed as the SEFD) varies significantly among them. The variety of antennas does not impact the data output obtained with the quality of our measurements as seen later in Figure 10.

The number of observations conducted by each antenna varied depending on the Mars visibility, antenna availability, and transmission times of MEX. The distribution of the amount of observations over the past 10 years is given in Figure 1. Most of the data collected in this study were observed with the KVAZAR network of VLBI antennas in Russia, including Svetloe, Zelenchukya and Badary, Hartebeesthoek in South Africa, the 12 and 30 m telescopes from Warkworth, New Zealand (Woodburn et al. 2015), and the five radio telescopes operated by the University of Tasmania. All the sessions conducted from 2019 and onwards were conducted with antennas in Hobart, Katherine, Yarragadee, and Ceduna.

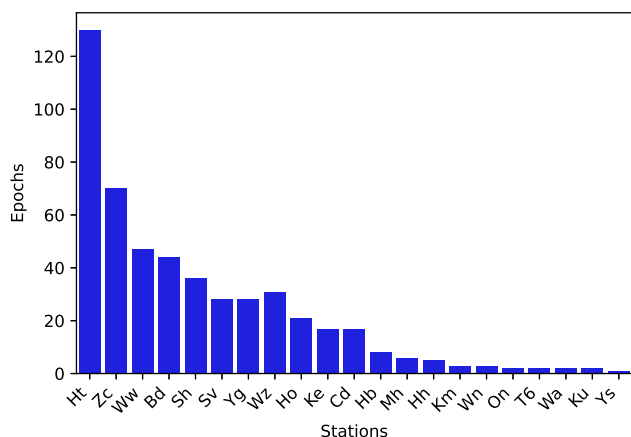


**Figure 1.** The distribution of number of observations conducted with each radio telescope between 2013 and 2020.

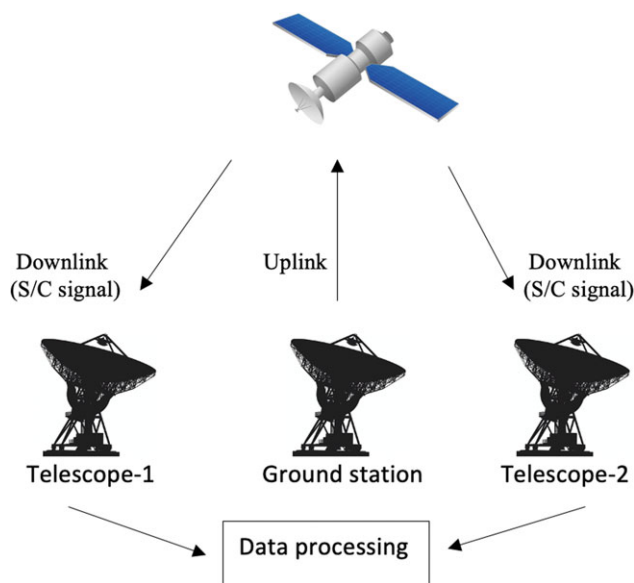


**Figure 2.** Observations conducted with PRIDE use the three way mode, in which the spacecraft is operating in two-way mode with ESTRACK stations and VLBI radio telescopes detect the signal in a third location.

The objective of these sessions was to quantify the phase fluctuations of the radio signal at different solar elongations. The observations covered the period between 2013 to 2020 an equivalent to three orbital periods of Mars. The onboard receiver system of MEX is capable of receiving and transmit radio signals in S-band and X-band utilising a high gain antenna. The communication is either a one-way link using the spacecraft's in-built ultra stable oscillator or a two-way link wherein an initial signal is transmitted from an Earth station which gets locked in the spacecraft and then re-transmitted to Earth (Asmar *et al.* 2005). For our observations, we used a three-way mode (Figure 2), a variation of the two-way, wherein the transmitting ground station is different to the receiving ground station. The receiving stations are generally equipped with hydrogen masers which provide better phase stability as accurate reference clocks.

Each session was segmented into scans of 19 min. This is adequate to deconstruct the phase fluctuations down to a milliradians resolution and keep consistent with Molera Calvés *et al.* (2014).

We record the broadband radio signal in VLBI specific data format (Whitney *et al.* 2009) in multiple frequency channels with bandwidths of 8, 16, or 32 MHz depending on the station's back-end configuration. For example, the latest digital back-end at the UTAS stations of Katherine and Hobart specifically supports 32 MHz bandwidth per channel, recording only linear polarised radio signals. The recorded raw files for each session consist of ten to hundreds of gigabytes depending on the session's length.

### 3.2. Data processing

The data obtained at individual telescope sites was either sent in its raw state or partially processed using the software pipeline and then sent across to the investigation centre by electronic or physical means. The received raw spacecraft files are processed through a high spectral resolution multi-tone Spacecraft Doppler tracking software (SDtracker) (Guifré Molera Calvés *et al.* 2021) to extract the topocentric frequency and residual phase of the spacecraft. The SDtracker comprises three major steps of Software spectrometer (SWspec), the Spacecraft tracker (SCtracker), and digital phase-locked loop (dPLL)<sup>a</sup> outlined below.

#### 3.2.1. SWspec

The first step in processing the data is to identify the channel containing the spacecraft carrier signal which is easily determined from the pre-existing transmission frequency information. In this step, a time-integration of the scan is performed wherein multiple spectra are generated which is given by  $N = LS/i$  where  $LS$  is the length of scan in seconds and  $i$  is the integration time in seconds. It is important to note here that the integration time used for processing the MEX signal (2 s) is shorter than that used for the VEX (5s) because the orbit of the MEX is such that it is rotating more rapidly compared to VEX thereby requiring more iterations (spectra) for better resolution. A procedure of window-overlapped add discrete Fourier transform (WOLA-DFT) is then performed on the data to obtain the shift in frequency across the spectrum. The shift is determined using a polynomial fit. Typically, in spacecraft detections we use a sixth-order polynomial fit but Ma *et al.* (2021) determined that fourth and fifth order profile fits give nearly similar results. Figure 3 shows an example of the detection of the MEX spacecraft signal and the fitted frequency shift profile.

#### 3.2.2 Multi-tone tracking and PLL

In this step, the phase of the spacecraft carrier tone is stopped and we get the Doppler corrections to resolve the tone to within a narrow mHz level. This is done using a time integration algorithm. From the obtained spectrum, a narrow window is selected around the spacecraft tone and subject to a 2nd order DFT-based algorithm which gives a Doppler-corrected spacecraft tone in a 1–2 kHz narrow bandwidth (Figure 4).

The obtained tone is passed to the dPLL software which runs high-precision iterations. The software calculates a new time-integrated spectra at every step, estimates a new set of phase polynomial fit, and then does the phase stopping of the spectra. The output at every step is a new filtered and down-converted signal associated with a residual frequency and phase. The output bandwidth phase of the detections post the dPLL processing has a Doppler noise less than a hundred mHz.

<sup>a</sup><https://gitlab.com/gofrito/sctracker/>.

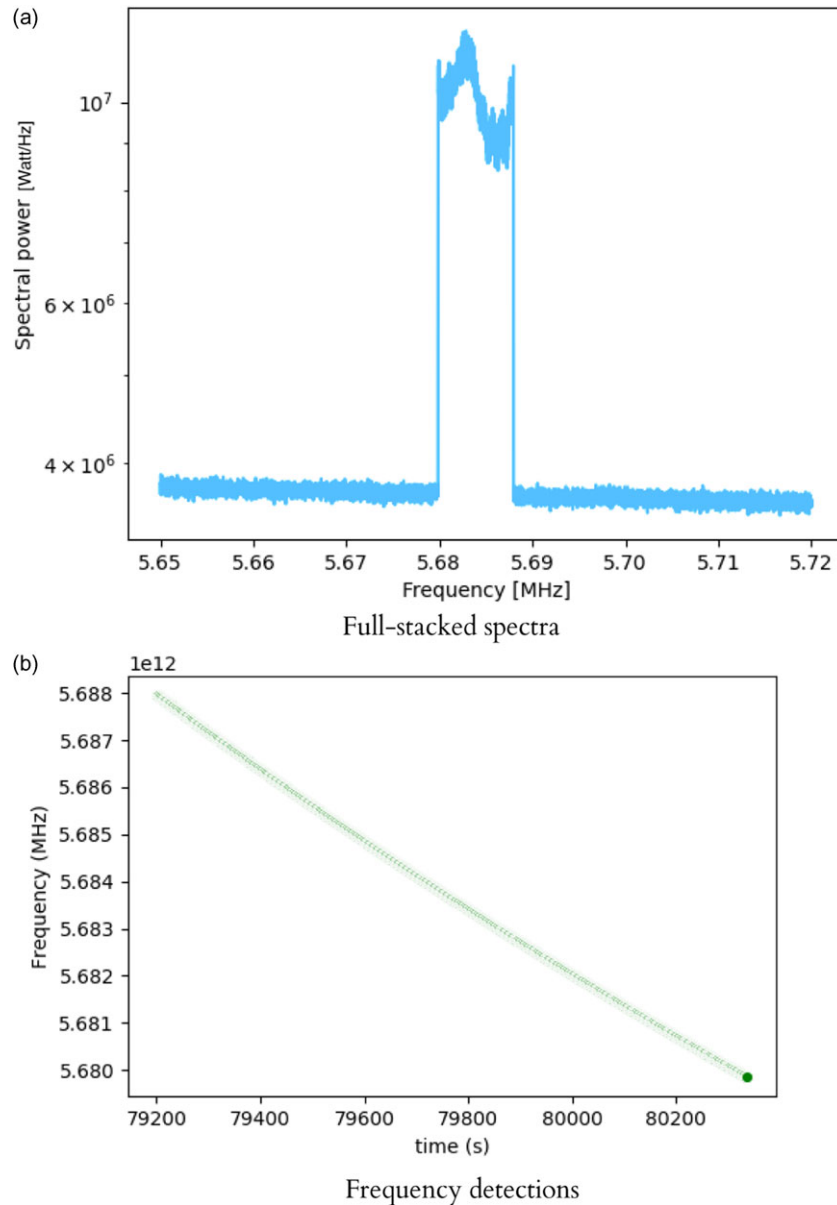


**Figure 3.** (a) Detection of the spacecraft carrier signal on the spectrum for a session held at Yarragadee. (b) The Doppler shift of the detected spacecraft tone over the course of the 19 min scan. We use a sixth order polynomial to fit the shift in the frequency tone.)

### 3.2.3 Scintillation analysis

In this final step of the data processing, we derive the temporal variation of the phase fluctuations over each scan and use the combined phase residuals of all session to estimate the phase scintillation indices. We start by plotting the residual phases for all the recorded scans. We inspect them looking for outlier, which mostly could be caused by a phase jump on the data. Depending on the spacecraft motion or low signal-to-noise ratio (SNR) the dPLL stage is not capable to unwrap perfectly the phase of the spacecraft. These jumps can sometimes be recovered by reducing the number of FFT points per segment in the dPLL. This may however not work when there is a short gap in the data caused by the recorder. In these outlier cases, we discard the scan and continue with the remaining data set.

The first step is to evaluate if the root mean square (*rms*) of phase fluctuations in radians is consistent in all the scans. The *rms* is actually the total energy of the phase fluctuations and it can be calculated as seen below.

$$E = \sum_j [\sigma^2 dt] \tag{8}$$

We can also express the power in time domain terms as:

$$P = \frac{E}{Ndt} \tag{9}$$

where  $E$  is the total energy,  $\sigma$  is the phase residual,  $j$  is the time scale spanning across the ' $N$ ' data points, and  $dt$  is the sampling interval.

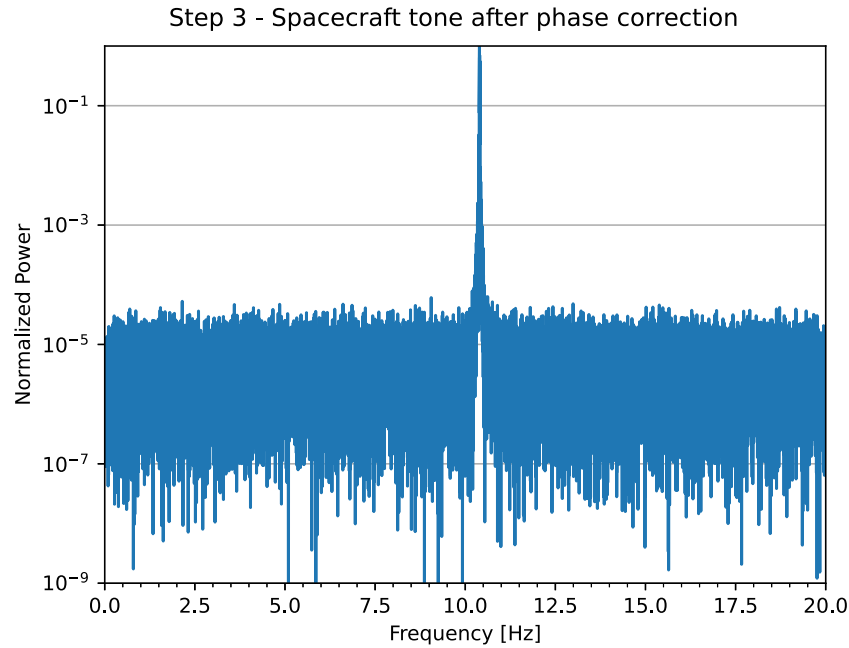


**Figure 4.** The narrow tone of the MEX carrier signal obtained after the digital phase-locked loop.

From this point, we are converting our time domain samples into frequency domain by using a windowed fast Fourier transformation. The phase power spectrum gives us an insight into the large-scale structure of the solar wind, showing in which range of frequencies the effect of plasma scintillation (scintillation band) is more prominent compared to the noise band. Determining the phase power spectral density involves a few steps.

We use two different forms of density spectra: windowed and unwindowed. We use the windowed spectra for estimation of the slope and relate it to a typical Kolmogorov spectrum. We use the unwindowed spectra for filtering and estimation of the scintillation *rms* and noise system *rms*.

$$psp = \mathcal{F}(\sigma) \quad (10)$$

$$pspw = \mathcal{F}(\sigma \cdot win) \quad (11)$$

where *pspw* is the windowed spectra and *psp* is the unwindowed spectra. The units are expressed in square radians per Hz. We calculate the power spectra for each of the scans and then we stack them all together.

$$pspw = \frac{1}{N_s} \cdot \left( \sum_j \frac{2 \cdot pspw}{BW} \right) \quad (12)$$

The scintillation caused by the plasma can be determined by doing a first-order approximation of the power spectral density given as

$$L_{ps} = c + mL_f \quad (13)$$

where  $L_{ps}$  is the average-windowed power spectral,  $m$  is the slope of the fitted line,  $L_f$  the frequency on logarithmic scale, and  $c$  is a constant. The limits of the best fit line are taken where the slope looks linear in the log-log scale. The red line in Figure 6 represents this line of fit. The slope is indicative of the spectral index which represents how the solar wind varies with phase.

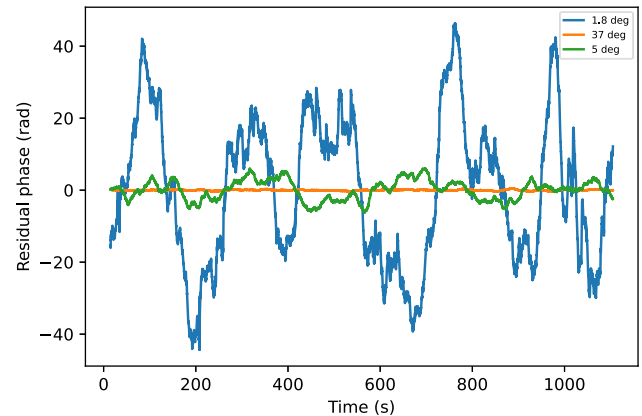


**Figure 5.** Phase fluctuation at different solar elongations (1.8 deg, 5 deg, and 37 deg) at Hartebeesthoek (Ht) on three different epochs (2015 June 8, 2015 July 9, and 2016 February 8, respectively).

We set frequency limits within the spectral density to distinguish between the contributions of scintillation and noise to phase fluctuations. The lower limit frequency for the scintillation band is taken as 0.003 Hz which represents the effective integration time while the upper limit is taken between 0.1 and 0.5 Hz depending on where the system noise band starts to dominate. These limits can be seen in Figure 6. The standard deviation of the phase fluctuation in the noise band determines the system noise level while the standard deviation of the phase fluctuation in the scintillation band (interplanetary plasma) gives the scintillation index.

## 4. Results

### 4.1. Analysis of the phase fluctuations

The phase of the spacecraft carrier signal is affected by the interplanetary plasma during both up and down-link transmissions.

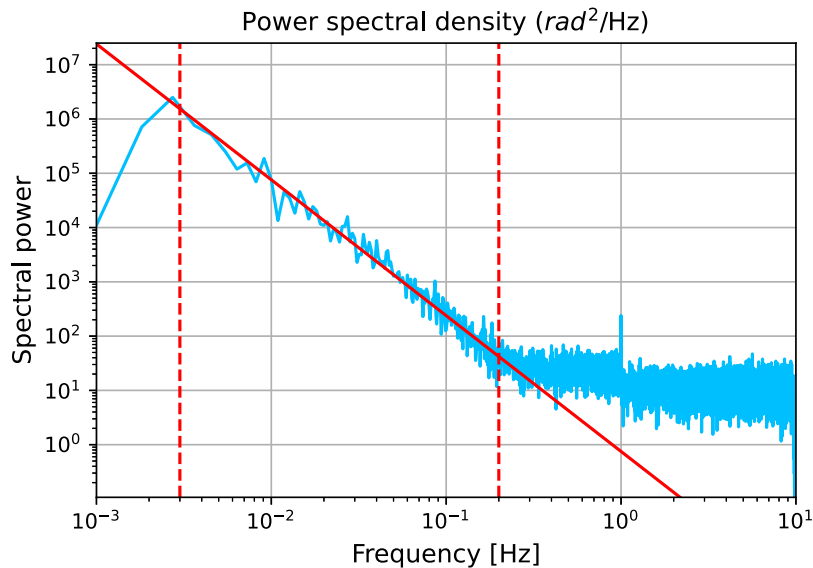


**Figure 6.** The power spectral density of a session held at Yarragadee on the 2020 April 13. The two horizontal dotted red lines encapsulate the scintillation band with the slope of the spectrum's fit (red line) corresponding to  $-2.431$ . The region beyond the second (right) dotted line corresponds to the noise band.

The scan duration (19 m) and number density of electrons are key factors that influence the value of the phase scintillation. Increasing the scan length increases the average phase residual values and for an optimum scan length to capture the long-scale structure of the solar wind we picked 19 min; it is the same duration Molera Calvés et al. (2014) chose for the observations of VEX thus allowing for a consistent comparison. The density of electrons increases at lower solar elongations and thus the expected trend of higher phase fluctuations at low solar elongations is consistent with our studies as seen in Figure 5. The blue line in the figure is an observation at the Hartebeesthoek station from the 2016 August 8 at a very low solar elongation angle (1.8 deg) which shows a high phase fluctuation while in contrast the green and yellow lines correspond to higher solar elongation angles of 5 deg and 37 deg respectively which demonstrate lesser phase fluctuation.

The contributions of the scintillation and the noise are differentiated by plotting a first-order approximation fit of the power spectral density on a logarithmic scale. The slope of the fit is indicative of the spectral index which is consistent with the Kolmogorov power spectrum of turbulence. The values of the slope of the spectral index for our observations ranged from  $-3.208$  to  $-1.374$  with a mean value of  $-2.43 \pm 0.11$ . This is similar to the value of  $-2.42 \pm 0.25$  obtained from previous VEX observations (Molera Calvés et al. 2014) and the value of  $-2.45$  found by Woo & Armstrong (1979). The slope is given as  $m = 1 - p$  where  $p$  is the Kolmogorov index. The average value of  $m = -2.42$  we obtain agrees with the  $p = 11/3$  from the earlier study of Kolmogorov (1991). Figure 6 shows the phase power spectral density from a session held at Yarragadee. The scintillation band shows the range of frequencies where the plasma is dominant (0.008–0.3 Hz) and the noise band is where the system noise effects start dominating.

The spectral index value calculated for each of the sessions is found to be independent of the scintillation. In Figure 7, we can distinguish the phase power levels for the low and high solar elongation spectra for the same station Yarragadee. The other noticeable feature is the dominance of the scintillation band over a longer frequency range in our lower solar elongation observation.

#### 4.2 Scintillation analysis of 3 orbital periods

We compare the scintillation indices at various solar offsets, the distance from closest point of approach from the line of sight of observation to the Sun. This gives an insight into how the signal is affected in proximity to the Alfvén surface which is at nearly 12 solar radii from the Sun (DeForest, Howard, & McComas 2014). We observe the phase scintillation for different solar offsets in Figure 8.

The intensity and phase variability are understood by calculating the power spectral density of each of the individual sessions we had. The contribution towards phase variability by each of phase scintillation and noise were calculated from within their respective bands as distinguished previously in Figure 6.

In Figure 9, we plot the scintillation values for each station at different solar elongation angles. The values for the scans below 10 degrees of elevation are omitted because these are saturated by the troposphere-induced scintillation. It can be seen that the lower solar offset indicates a higher perturbation in phase. Figure 9 reiterates the idea phase fluctuations at lower solar elongation ( $<5$  deg) by nearly 40–60 times than at higher solar elongations (Molera Calvés et al. 2014).

The size and sensitivity of the individual telescopes do not affect the readings of the phase scintillation value. For this purpose, the carrier line SNR was compared against both the scintillation index and Doppler detection noise (2–10 s integration time) as shown in Figure 10. We performed a regression analysis to find that both the scintillation index and Doppler noise are unaffected by the carrier line SNR. The statistical test for both sets of quantities returned an  $r$ -value of  $-0.1$  indicated they are strongly uncorrelated. The outliers we see in the Doppler noise (above 200) are from a couple of epochs; Hartebeesthoek had a session (2015 June 8) where the solar elongation was lesser than 2 degrees while Svetloe and Zelenchukskaya had a session (2015 May 22) where the solar elongation was about 6 degrees. The scintillation index has the same sessions as the outliers (above 15) with the addition of another session from Svetloe, Zelenchukskaya, and Sheshan (2015

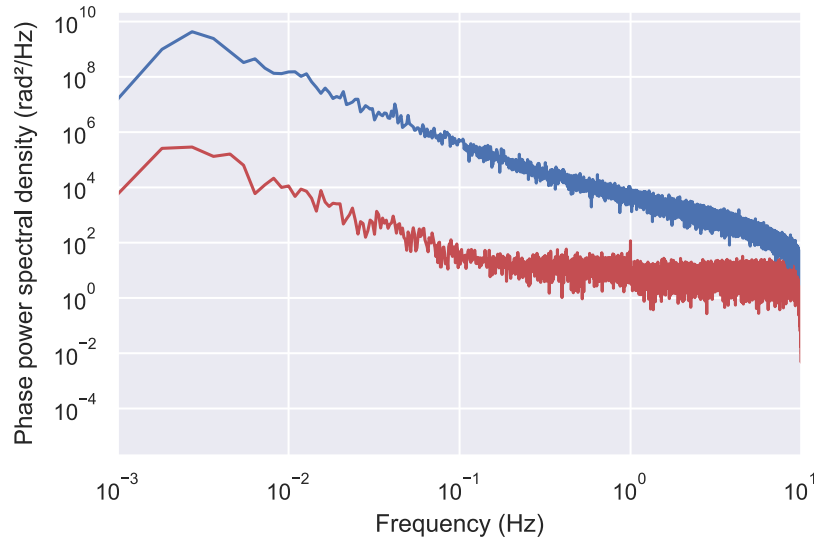


**Figure 7.** The power spectral density of two sessions held at Yarragadee where the blue spectrum is when the solar elongation was 4.8 deg and the red spectrum is when the solar elongation was 87.3 deg.

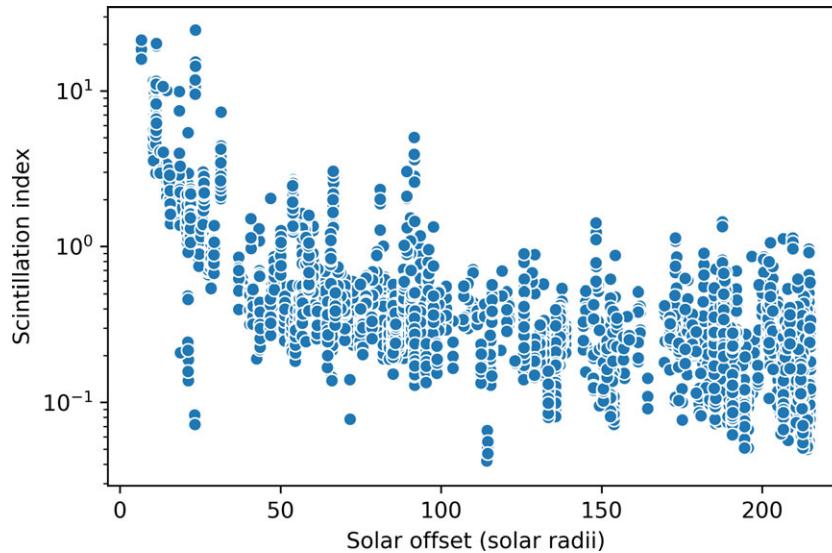


**Figure 8.** An overview of the scintillation index variation at different solar offsets. We see that the values remain fairly low and constant at solar offsets beyond 12 solar radii. The spikes we see near 90 solar radii correspond to a coronal mass ejection (CME) event on the 2015 April 6 (Molera Calvés et al. 2017).

June 25). It is possible that there was an issue with the backend baseband converters during the experiment.

The TEC of the interplanetary plasma along the line of sight from Earth to the Mars Express spacecraft is determined by integrating the electron density values obtained at points along the path of Earth and Mars for an initial value of the solar wind velocity. We aim to find the best fit of the theoretically determined model with the observations. We use a scaling factor  $K$  to relate the phase scintillation with the TEC which is an empirically determined constant lying between 2 000–4 000. We derive the relation from (2) to be:

$$TEC = K \cdot \sigma \tag{14}$$

The best value for  $K$  is calculated to be 2 390 from the weighted mean of the conversion factor for the best-fit scenario obtained for

each point individually. Figure 11 depicts the TEC corresponding to various factors within our observations.

The obtained TEC value is a combination of propagative effects of the plasma, ionosphere, and mechanical and thermal noises from the instrumentation. The cumulative effect from each of these contributions can be described by the following equation:

$$Scint = \sqrt{TEC_{sw} \cdot k_{sw}^2 + TEC_{ion} \cdot k_{ion}^2 + PCa^2 + Bpr^2 + Airm^2} \tag{15}$$

where  $Scint$  is the measured scintillation by a single dish antenna, the  $TEC_{sw} \cdot k_{sw}$  is the theoretical interplanetary two-way TEC accounting for fast, slow and mean solar speeds times a scaling factor to convert from radians per tec unit, the  $TEC_{ion} \cdot k_{ion}$  is the

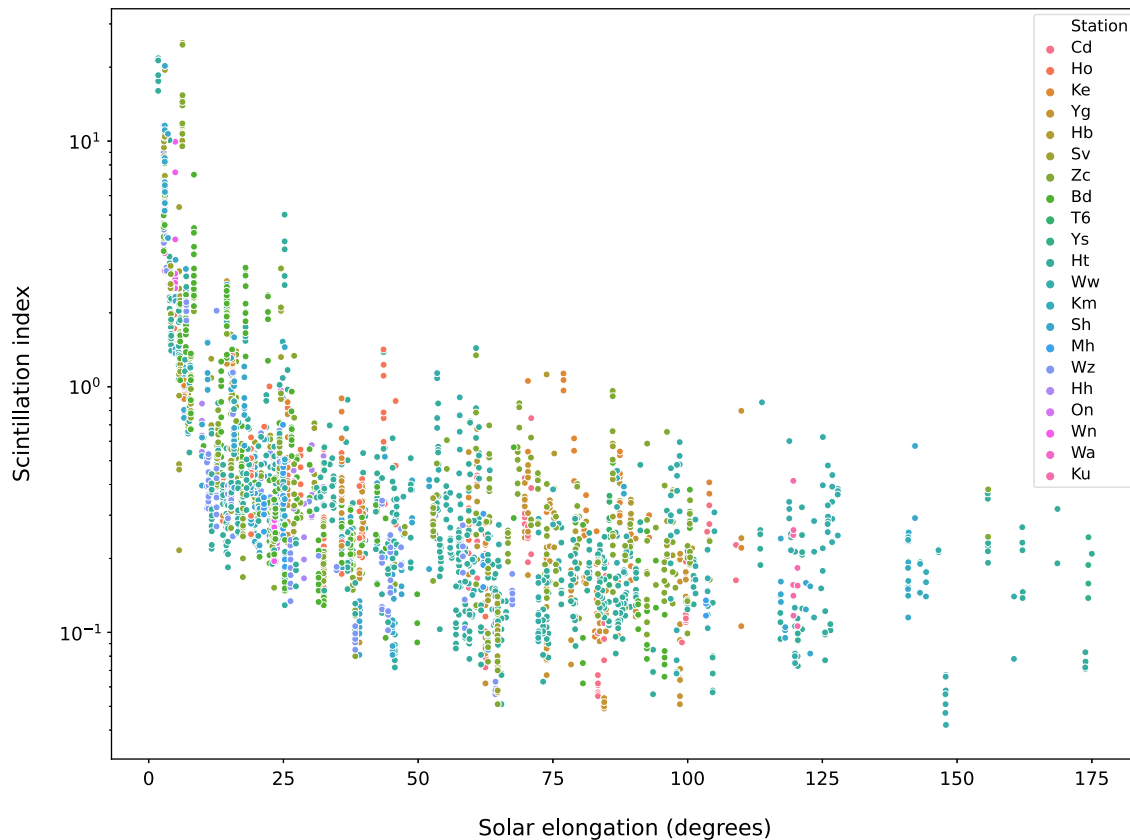


**Figure 9.** The scintillation index variation with solar elongation at different stations is described in the plot. The solar elongation describes the angle between the Sun, Earth, and the spacecraft; indicating that the radio signals with lower solar elongation are more closely aligned to the Sun's emissions. We can see that there is almost a ten fold increase in the scintillation at a lower solar elongation.

theoretical ionospheric two-way TEC times a scaling factor to convert from radians per tec unit,  $P_{Cal}$  is the instrumental phase error derived from the Phase Calibration measurements,  $B_{pr}$  is the base phase variation due to the Allan variance of the transmission and receiving H-maser clocks, and the  $A_{irm}$  is the two-way air mass in units of  $1 \text{ kg cm}^{-2}$

The  $P_{Cal}$  phase error was set to 0.0295 radians for those observations we did not have measurement data. The rest of the sessions the phase error was extracted directly from the measurements of these tones. We had the phase cal tones present in selected sessions to verify both independent measurements. However in standard observations they are disabled to decrease additional noise. Therefore, they are usually not estimated.

## 5. Discussion

The study involved tracking the Mars Express radio signal from 2013 to 2020 to study the interplanetary plasma. We measured the scintillation indices at different solar elongations from the carrier phase. The spectral index derived from the phase power spectrum returns a value of  $-2.43 \pm 0.11$  which is in agreement with the turbulent media described by Kolmogorov (Kolmogorov 1991).

We fitted the data obtained with MEX measurements to the theoretical model of TEC. We compared the results with the measurements published by VEX and improve our model. (Molera Calvés et al. 2014). A core objective of this paper is to test our theoretical models of the TEC by comparing to the observed TEC. The

first step was to remove the contributions from the ionosphere and the system noise because this study is concerned with the contributions due to the solar wind alone. We see an improvement of 1.8% in the fit which shows. These newly obtained data points are overlaid with the theoretical fit as shown in Figure 12.

The prediction of the theoretical fit breaks down at higher solar elongations. One of the expected reasons is the speed of the solar wind which is a variant across time and direction where the ionospheric effects dominate. The second reason which could possibly explain the observed points being higher (than the prediction) at larger solar elongations is the correlation of the uplink and downlink signals. The effective variance of the two time series for the uplink and downlink signals is given as

$$\sigma_{eff}^2 = \sigma_u^2 + \sigma_d^2 + 2 * covariance(u, d). \quad (16)$$

The inhomogenous structure of plasma and the associated wind speed would mean that the uplink and downlink signal traverse through different segments of the large-scale plasma structure. Thus, the uplink and downlink contributions are uncorrelated implying  $covariance(u, d) = 0$ . However, in cases when the solar elongation is close to 180 degrees, it is possible the solar wind ( $200\text{--}800 \text{ km s}^{-1}$ ) is moving along the direction similar to that of the signal transmission ( $3 \times 10^5 \text{ km s}^{-1}$ ) as depicted in Figure 13. If this is the case, the uplink and downlink signals could pass through similar plasma regions, resulting in partial correlation. This would make the covariance term non-zero leading to an

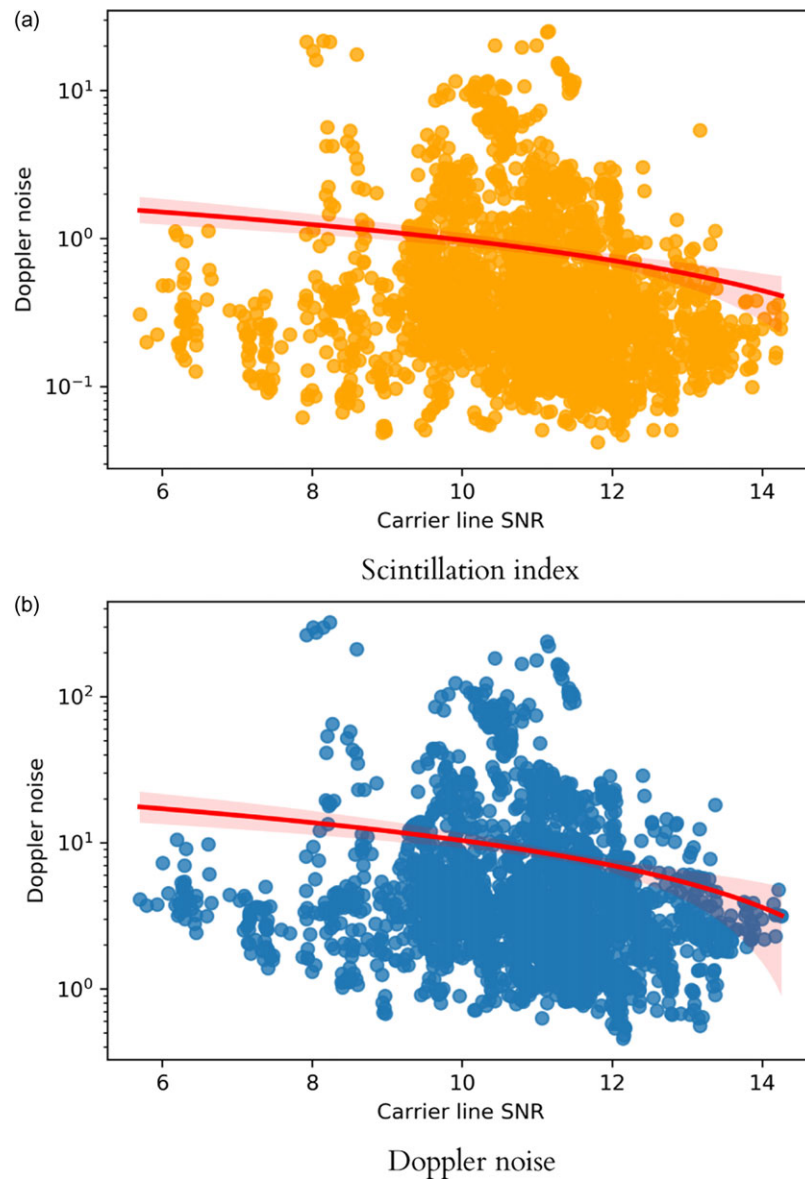


**Figure 10.** The above two regression plots describe how the scintillation index (top) and the Doppler detection noise (bottom) vary with carrier line SNR. The red line is the line with least sum of squares of errors and is the best fit for the regression.

increase in observed TEC value and thus explain the points being above the theoretical predictions at high solar elongations.

Having presented an improved quantitative analysis of interplanetary plasma from single dish observations, we look to further advance the technique and characterise plasma by using different line of sight observations. This would involve using multiple stations simultaneously and concurrent observations of multiple spacecraft (Ma *et al.* 2021). The study focused on long-term series analysis of phase scintillation on multiple line of sights with the same target. These phase signatures will benefit to achieve higher orbit determination accuracy on upcoming missions like JUICE.

Another interesting domain to look into is the locational aspect of the magnetic and plasma field of the solar wind. Plasma sheets in the Sun's magnetosphere are regions of enhanced plasma with

the neutral sheet; the latter are storehouses of magnetic and plasma energy released periodically (Mishin & Streltsov 2021). The position of the spacecraft determines which regions of the magnetosphere the radio signal traverses. Kim *et al.* (2020) noticed an increase in the count of ions and electrons when Juno made plasma sheet crossings. We could see minor jumps in our TEC if our radio signal made these crossings. Observing multiple targets simultaneously (MEX, BepiColombo, Tianwen (Ma *et al.* 2022), JUICE)<sup>b</sup> could provide insight into where such sheet crossings are located and is a study worth further investigating. This could consequentially help explain the increased TEC as seen in our observations compared to the theoretical model.

<sup>b</sup><https://sci.esa.int>.

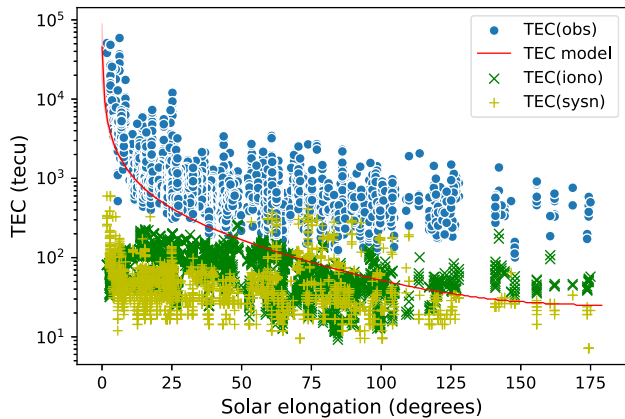


**Figure 11.** In this plot we see the total electron content contributions from various factors and how it compares to the theoretical fit of the model (nominal speed in this case).

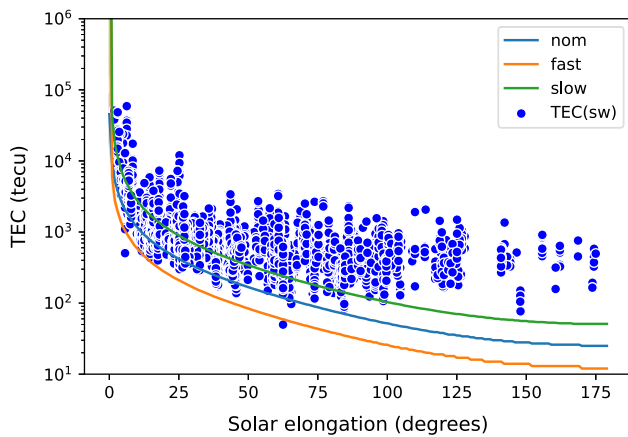


**Figure 12.** The blue points represent the measured values of TEC from our observations and the red line is the trend of the TEC as predicted by the theoretical model ( $n_e = 2.15 \times 10^6$ ). The prediction fails at higher elongation where the data points are significantly above the theoretical fit for nominal, slow, and fast solar wind speeds.

**Acknowledgement.** This study was possible thanks to the observations carried out by the different operators across the array of EVN telescopes in China, Europe, Russia, Africa, and the AUT University (for Ww and Wa). The long-term study of plasma was also consolidated by the array of the Auscope VLBI telescopes operated by the University of Tasmania. The author acknowledges the valuable input from collaborators in JIVE and Shanghai Astronomical Observatory which helped improve the quality of the work. The collection of the data for research was possible thanks to the ESA’s MEX communication team.

**References**

Acosta, R., Nessel, J. A., & Morse, J. R. 2010, Path Length Fluctuations Derived from Site Testing Interferometer Data. National Aeronautics and Space Administration, Glenn Research Center  
 Ando, H., et al. 2015, *JGR*, 120, 5318  
 Asmar, S., Armstrong, J., Iess, L., & Tortora, P. 2005, *RSci*, 40  
 Beasley, A., & Conway, J. 1995, in *Very Long Baseline Interferometry and the VLBA*, 327  
 Bocanegra-Bahamón, T., Molera Calvés, G., Gurvits, L., Duev, D., Pogrebenko, S., Cimo, G., Dirxk, D., & Rosenblatt P. 2017, arXiv preprint [arXiv:1709.03419](https://arxiv.org/abs/1709.03419)  
 Bocanegra-Bahamón, T., et al. 2019, *A&A*, 624, A59

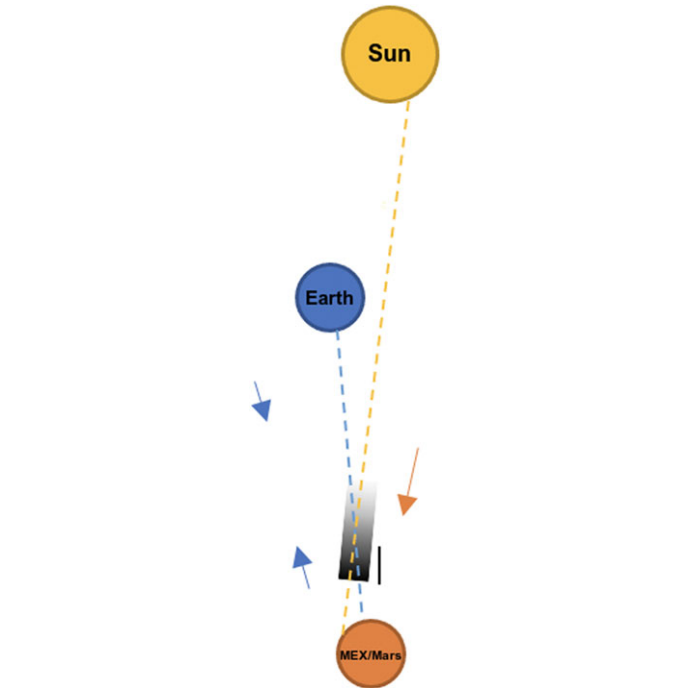


**Figure 13.** A two-dimensional model of transmission of the satellite signal and the solar wind direction. The yellow sphere is the Sun, the blue sphere (Earth) is the observer and the red sphere is the target (MEX). The blue arrows represent the direction of the uplink and downlink while the yellow arrow is the direction of the solar wind. The black and white slab represent the oscillating density fluctuation as a slab. The path of the solar wind would be a chain of multiple such slabs but varying in their fluctuation pattern due to solar wind’s inhomogenous nature.

Boyd, B., et al. 2022, *JSWSC*, 12, 34  
 Conroy, J. P., Deshpande, K., Scales, W., & Zaghoul, A. 2022, *RSci*, 57, e2021RS007259  
 Crane, R. K., 1977, *PIEEE*, 65, 180  
 Davies, K. 1990, *Ionospheric Radio*, Vol. 31 (IET)  
 DeForest, C., Howard, T., & McComas, D. 2014, *ApJ*, 787, 124  
 Duev, D. A., Calvés, G. M., Pogrebenko, S. V., Gurvits, L. I., Cimo, G., & Bahamon, T. B. 2012, *A&A*, 541, A43  
 Duev, D. A., et al. 2016, *A&A*, 593, A34  
 Edmondson, J. 2012, *SSR*, 172, 209  
 Hassler, D. M., Dammasch, I. E., Lemaire, P., Brekke, P., Curdt, W., Mason, H. E., Vial, J.-C., & Wilhelm, K. 1999, *Sci*, 283, 810  
 Holdaway, M., Radford, S. J., Owen, F., & Foster, S. M. 1995, *ALMA Memo* bf, 129  
 Jin, S., Park, J.-U., Cho, J.-H., & Park, P.-H. 2007, *JGRA*, 112  
 Karasawa, Y., Yamada, M., & Allnutt, J. E. 1988, *IEEE TAP*, 36, 1608  
 Keihm, S. J., Janssen, M. A., & Ruf, C. S. 1995, *IEEE TGRS*, 33, 147  
 Kim, T. K., et al. 2020, *JGRSP*, 125, e2019JA027696  
 Kolmogorov, A. N. 1991, *PRLSA*, 434, 9  
 Ma, M., et al. 2021, *AJ*, 162, 141  
 Ma, M., et al. 2022, arXiv preprint [arXiv:2210.10324](https://arxiv.org/abs/2210.10324)  
 MacMillan, D., & Ma, C. 1994, *JGRSE*, 99, 637  
 Manoharan, P., Ananthakrishnan, S., Dwyer, M., Detman, T., Leinbach, H., Kojima, M., Watanabe, T., & Kahn, J. 1995, *SoPh*, 156, 377  
 Mishin, E., & Streltsov, A. 2021, *Nonlinear Wave and Plasma Structures in the Auroral and Subauroral Geospace* (Elsevier)  
 Molera Calvés, G., et al. 2014, *A&A*, 564, A4  
 Molera Calvés, G., et al. 2017, *SW*, 15, 1523  
 Molera Calvés, G., Pogrebenko, S. V., Wagner, J. F., Cimò, G., Gurvits, L. I., Bocanegra-Bahamón, T. M., Duev, D. A., & Nunes, N. V. 2021, *PASA*, 38  
 Narayan, R. 1992, *PTLRL*, 341, 151  
 Owens, M. J., & Forsyth, R. J. 2013, *LRvSp*, 10, 1

- Pinto, R. F., & Rouillard, A. P. 2017, *ApJ*, 838, 89
- Schwenn, R. 1990, in *Physics of the Inner Heliosphere I* (Springer), 99
- Smyth, J., & Trolese, L. 1947, *PIRE*, 35, 1198
- Vasseur, H. 1999, *IEEE TAP*, 47, 293
- Wexler, D. B., Hollweg, J. V., Efimov, A. I., Lukanina, L. A., Coster, A. J., Vierinen, J., & Jensen, E. A. 2019, *ApJ*, 871, 202
- Whitney, A., Kettenis, M., Phillips, C., & Sekido, M. 2009, in *The 8th International e-VLBI Workshop*, 042
- Woo, R., & Armstrong, J. 1979, *JGR*, 84, 7288
- Woodburn, L., Natusch, T., Weston, S., Thomasson, P., Godwin, M., Granet, C., & Gulyaev, S. 2015, *PASA*, 32
- Yakovlev, O. I. 2002, *Space Radio Science* (CRC Press)